https://dx.doi.org/10.1016/j.apenergy.2021.118366

Optimizing the charging protocol to address the self-discharge issues in rechargeable alkaline Zn-Co batteries

Wenxu Shang[a], Wentao Yu[a], Xu Xiao[a], Yanyi Ma[a], Ziqi Chen[a], Meng Ni[b], Peng Tan[a,]*

a. Department of Thermal Science and Energy Engineering, University of Science and Technology of China (USTC), Hefei 230026, Anhui, China.

b. Department of Building and Real Estate, Research Institute for Sustainable Urban Development (RISUD) & Research Institute for Smart Energy (RISE), The Hong Kong Polytechnic University, Hung Hom, Kowloon, Hong Kong, China.

*Corresponding author: pengtan@ustc.edu.cn

Abstract

Aqueous rechargeable Zn-Co batteries feature intrinsic safety and excellent electrochemical performance, and zinc metal is cheap with abundant reserves. However, a key issue, self-discharge, which may be fatal to the application, is always overlooked. Herein, the self-discharge performance is investigated systematically for the first time, and in-depth charge-discharge mechanisms are analyzed. Based on a free-standing Co_3O_4 electrode, the insufficient utilization of the active material is found under a conventional galvanostatic charging process. Additionally, a dramatic attenuation in the open-circuit voltage is exhibited during the delay, leading to poor capacity retention. Through electrochemical tests and ex-situ characterization, the limited capacity and the severe self-discharge behavior are ascribed to the low amount and poor stability of the high valence state, respectively. Aiming at suppressing the self-discharge behavior, a novel charging protocol is proposed based on a new mechanism, which uses a time-controlling potentiostatic charging after the galvanostatic charging process. Using this strategy, the discharge capacity increases effectively by about 31.8% from 220 to 290 mA h g^{-1}, and the capacity retention ratio after 10 h delay lifts from 72% to 90%. More importantly, the discharge capacity remains 100% after even 2500 cycles. This work puts forward a practical method for the operation of Zn-Co batteries, addresses the limiting issues for application, and greatly facilitates the improvement of this technology. Further, the results also inspire the research of other rechargeable Zn-based batteries.

Keywords: Zn-Co batteries; charging protocol; high capacity; low self-discharge rate

1. Introduction

Fast energy consumption propels the development of energy storage technologies. Li-ion batteries have successfully obtained commercialization due to their high operating voltage, energy efficiency, and good cycle stability [1–3]. Nevertheless, the intrinsic limited energy density, poor safety guarantees, and high cost hinder further development [4–6]. On the other hand, Zn-based batteries (e.g., Zn-Mn, Zn-Ni, Zn-Co, and Zn-Ag batteries) [7–12], which are characterized by the high theoretical capacity (820 mA h g_{Zn}^{-1}), environmental friendliness, and low cost, have gradually come into the view.

As an emerging type, the rechargeable Zn-Co battery based on Co_3O_4 was proposed by Wang et al., which presents a high theoretical capacity of 446 mA h g^{-1} and a high operating voltage of ~1.8 V [13]. However, the practical capacity is only 162 mA h g^{-1}, which leads to the low energy density of 241 Wh kg^{-1}. Aiming at improving the utilization of active material and cycle stability, tremendous fruits have been collected from microstructure, oxygen defects, and element doping [14–16]. Tan et al. reported a Zn-Co battery with Co_3O_4 nanowire, which delivers a capacity of 173.6 mA h g^{-1} [17]. By turning the microstructure into the heterogeneous porous nanowire, Shang et al. increased the electrical conductivity and reaction surface to successfully improve the capacity to 230 mA h g^{-1} [18]. By introducing oxygen defects, Wang et al. fabricated the Co_3O_{4-x} bubbles, which deliver a high discharge capacity of 369.4 mA h g^{-1} due to the enhanced electric conductivity and unique structure [19]. In terms of doping strategy, Shang et al. partially substituted Co with Ni in Co_3O_4 and changed the morphology into a multiple self-assembled nanowire-nanosheet structure, increasing the capacity and energy density to 272 mA h g^{-1} and 448 W h kg^{-1}, respectively [20]. Li et al. doped Zn in Co_3O_4 nanowire, which effectively enhanced the conductivity, leading to a remarkable capacity of 1.25 mA h cm^{-2} [21]. Additionally, Xie et al. integrated the $NiCo_2O_4$, $CoMoO_4$, and Co_3O_4 into one hierarchical structure, the high electrical conductivity and reaction surface facilitates the electron and ion transfer, endows an ultrahigh areal capacity of 2.51 mA h cm^{-2} and an energy density of 4.09 mW h cm^{-2} [22].

Based on the redox reactions of Co_3O_4, the valence state varies between $Co^{2+} \leftrightarrow Co^{3+} \leftrightarrow Co^{4+}$ during charging and discharging [23,24]. Even with these efforts, however, the current capacity for Co_3O_4 is still far below the theoretical value considering the valence state change. Previous works have indicated that the reaction between $Co^{3+} \leftrightarrow Co^{4+}$ is much more difficult to occur compared to $Co^{2+} \leftrightarrow Co^{3+}$ [25,26]. Additionally, the redox pair of Co^{3+}/Co^{4+} is unstable because of the rapid degradation from Co^{3+} to Co^{2+} [27]. More importantly, the initial valence state of Co is ~2.67 for the Co_3O_4, which means that the utilization of valence state variation from Co^{3+} to Co^{4+} is very limited, while the majority of the practical capacity is from Co^{2+} to Co^{3+}. Thus, the lack of the high valence state causes insufficient utilization. Although the reported Zn-Co batteries can deliver the output-voltage of up to 1.8 V, the region is very limited with the main voltage plateau of ~1.65 V, which also demonstrates the insufficient valence state transformation [24].

The above-mentioned issue of Co_3O_4 has questioned the ignored self-discharge behaviors in Zn-Co batteries, which have been widely reported in supercapacitors [28–30]. Under the charged state, the self-discharge will cause the transition from the high state to the lower one, decreasing the discharge capacity due to the lack of a high voltage region [31]. The capacity loss can be recovered only after charging again, and the “driving force” of self-discharge for supercapacitors is the Gibbs free energy [32], in which the mechanisms are summarized as charged redistribution caused by the migration of charged state ions adsorbed on the electrode, redox reaction attributed to the overcharge, and ohmic leakage between two electrodes [31,33,34]. To suppress the self-discharge behavior of supercapacitors, tremendous work has been reported. For example, Xia et al. added the nematic liquid crystal 4-n-pentyl-40-cyanobiphenyl (5CB) into the electrolyte to inhibit ions and redox species diffusion [33]. Peng et al. reported a membrane made from polyacrylonitrile with sodium dodecyl benzene sulfonate (PAN@SDBS) nanofibers, which slows the ion diffusion resulting from the concentration gradient [34]. Wang et al. modified the porous cellulose separator of carbon-based supercapacitor with a cationic polyelectrolyte and also restrains the ion diffusion [29]. Chen et al. used an ion-exchange membrane as the separator in the active electrolyte-enhanced supercapacitors (AEESCs), in which the migration of the active electrolyte was constrained [35]. Nevertheless, the suppression effect is limited and the self-discharge is still severe after these optimizations. However, the current research of Zn-Co batteries almost focuses on the active materials and electrochemical performance (i.e., discharge capacity, rate performance, and cycling stability), while the self-discharge is often overlooked and has been seldom reported to the best of our knowledge [36–38]. As for the self-discharge behavior of Zn-Ni batteries, some reasons have been reported, such as the reduction from NiOOH to $Ni(OH)_2$, oxygen gas evolution, and phase change [39]. In practical applications, the research on self-discharge is of great importance. A high self-discharge rate could cause a rapid voltage drop during the delay, leading to the poor practical discharge capacity, which will hinder the usage and waste the energy severely. Hence, this issue drastically impacts the commercialization of Zn batteries. In the field of electric vehicles (EV), the severe self-discharge after delay for several days will decrease the practical cruising ability, which could even be exacerbated in a warm climate [40–43]. For other electronic devices (e.g., mobile phones), the self-discharge requires frequent recharge to meet the daily use, which brings great inconvenience [44,45].

Herein, the self-discharge behavior of a Zn-Co battery was investigated systematically for the first time. The possible reasons corresponding to the voltage attenuation and the underlying reaction mechanism during discharging and charging processes were proposed. To suppress the self-discharge, a new charging protocol was proposed and great performance improvement was achieved. Further, the limiting factor for the low utilization ratio of Co_3O_4 in a Zn-Co battery was identified, and an ultra-high capacity was achieved.

2. Experimental Section

2.1 Preparation of the Co_3O_4 electrode

The Co_3O_4 electrode was fabricated by a hydrothermal process, followed by the heat treatment to form a free-standing nanowire structure on the nickel foam [18]. Briefly, 1 mmol of $Co(NO_3)_2 \cdot 6H_2O$, 4.5 mmol of NH_4F, and 8 mmol of $CO(NH_2)_2$ dissolved with 40 mL of water were mixed into an autoclave of 50 mL, and the clean Ni foam (3 cm × 5 cm) was put into it. After that, it was maintained under 120 °C for 9 h and calcined in the air under 350 °C for 3 h with a heating rate of 1 °C min^{-1}. The mass loading was measured to be ~2.2 mg cm^{-2}. After fabrication, the material characterization was conducted at the Experimental Center of Engineering and Material Sciences in USTC. Briefly, the morphology was observed by a scanning electron microscope (SEM, XL-30 ESEM), field emission transmission electron microscopy (TEM, JEM-2100F), and high-resolution TEM (HRTEM) images. The specific surface area and the corresponding pore volume were tested by the nitrogen adsorption-desorption isotherms using a Tristar II 3020M surface area and porosity analyzer. The valence states of Co of the samples were analyzed by X-ray photoelectron spectroscopy (XPS, ESCALASB 250 Xi, Thermo Scientific, USA) using Al monochromatic X-ray at a power of 150 W.

2.2 Electrochemical measurement

A Zn-Co battery was assembled with the positive electrode pouched from the prepared sample (diameter: 10 mm), the negative electrode of a Zn plate (thickness: 0.5 mm), and the aqueous electrolyte of 6 M KOH with 0.2 M $Zn(Ac)_2$ solution, which can ensure the excellent conductivity and the reversible reaction of the Zn electrode. The cycle voltammetry (CV) was tested in a two-electrode system by an electrochemical workstation (Solartron EnergyLab) in the potential range of 1.4 and 1.9 V (vs. Zn) with the scan rates from 0.2 to 1.0 mV s^{-1}. The pseudocapacitance performance was evaluated by the following formula [46]:

$$i = av^{b} \tag{1}$$

where i and v represent the peak current (mA) and scan rate (mV s^{-1}) of the CV curves, respectively, a is a constant value, b-value (0.5–1) is used to qualitatively evaluate the pseudocapacitive proportion, which can be obtained by fitting the correlation between $\ln i$ and $\ln v$ at each redox peak. The pseudocapacitive contribution and battery contribution can be calculated based on the following formula:

$$i=k_1v+k_2v^{1/2} \tag{2}$$

where k_1 and k_2 are constant values, and k_1v and $k_2v^{1/2}$ represent pseudocapacitive contribution and battery contribution, respectively. Electrochemical impedance spectroscopy (EIS) was conducted with an amplitude of 5 mV in the frequency range of 1000 kHz to 0.1 Hz. The battery performance and self-discharge behavior were tested by the charge-discharge tester (Neware, Shenzhen) under the voltage regions of 1.4 to 1.9, 1.8, 1.7, and 1.6 V with different delay time. The cycling stability was tested under the current density of 2 A g^{-1} based on the loading of Co_3O_4.

3. Results and discussion

3.1 Characterization and electrochemical analysis of the Co_3O_4 electrode

Free-standing Co_3O_4 on the nickel foam was applied as the positive electrode in this study. As shown in Fig. 1a, Co_3O_4 nanowires with an average length of ~4 μm are distributed uniformly. The TEM images in Fig. 1b illustrate a single nanowire with a diameter of ~120 nm, from which the constructed nanoparticles can enlarge the specific surface area. Figs. S1 and S2 give the nitrogen adsorption-desorption isotherms and the corresponding pore size distribution of the Co_3O_4 electrode. The specific surface and the pore volume are calculated to be 9.81 m^2 g^{-1} and 0.0238 cm^3 g^{-1}, respectively. Since the multiple pore size distributions (~2, 3-4, and 5-10 nm) are exhibited, this nanowire electrode has porosity. Moreover, the SEM and TEM images in Figs. S3 and 1b also indicate that the Co_3O_4 nanowire is composed of nanoparticles, further exhibiting its porosity. To investigate the pseudocapacitance of Co_3O_4, the CV curves in Fig. 1c demonstrates four redox peaks: Peak 1 at ~1.7 V and Peak 2 at ~1.6 V represent $Co^{2+} \rightarrow Co^{3+}$ and $Co^{3+} \rightarrow Co^{2+}$, respectively, while Peak 3 at ~1.85 V and Peak 4 at ~1.7 V correspond to $Co^{3+} \rightarrow Co^{4+}$ and $Co^{4+} \rightarrow Co^{3+}$, respectively [24,47,48]. Fig. 1d fits the correlation between ln*i* and ln*v*, from which the *b*-value for Peak 1 and Peak 2 is 1.0 and 0.94, respectively. According to eq 1, the values near 1.0 demonstrate a large proportion of pseudocapacitive contribution. Fig. 1e displays the pristine CV curve and the fitted pseudocapacitive contribution marked with the shaded area at 1.0 mV s^{-1}. Noted that the accuracy of the pseudocapacitive contribution is related to the CV curves. Since the scan rates used in the CV curves are ultralow, the number of test points is small, leading to the rough curves. Therefore, the fitted pseudocapacitive contribution curves show irregular shapes [22,27], while the results can also represent the changing trend. Based on eq. 2, the k_1v can be calculated to be 93.97%. When the scan rate changes from 0.2 to 0.4, 0.6, 0.8, and 1.0 mV s^{-1}, the value increases from 86.70% to 89.78%, 90.27%, 92.11%, and 93.97%, respectively (Fig. 1f and Fig. S4). This high proportion is similar to previously reported metal oxidation in the alkaline solution [27], indicating the pseudocapacitive contribution control, which may affect the valence retention ability during the delay.

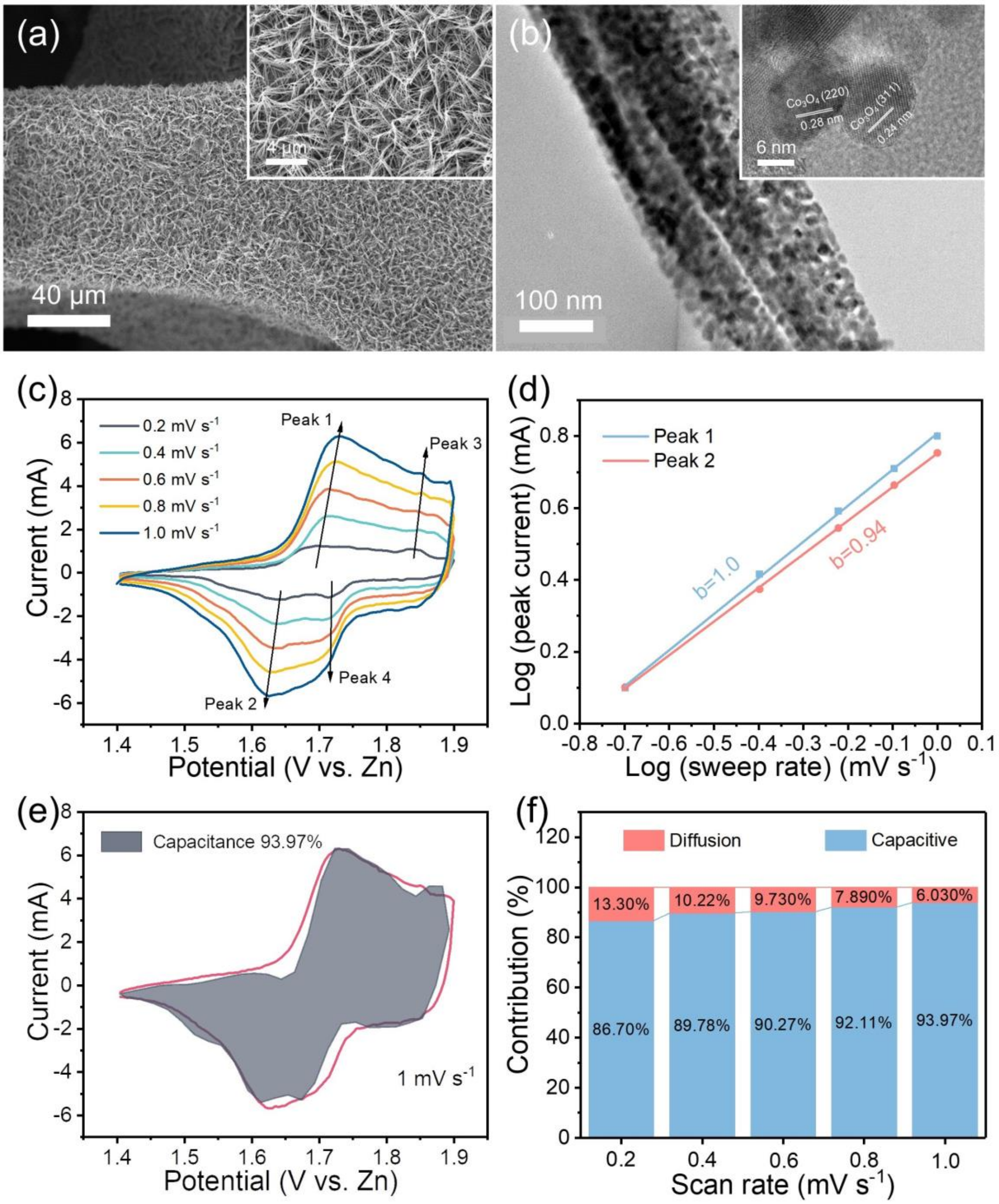

Fig. 1. (a) SEM images and (b) TEM images of Co_3O_4, and the insets show the high-magnification images. (c) CV curves of Co_3O_4 at various rates and (d) the corresponding fitted *b*-values at different redox peaks. (e) CV curve of Co_3O_4 at 1 mV s^{-1} and the corresponding pseudocapacitive contribution (shaded area). (f) Normalized contribution proportions of capacitance and diffusion at various scan rates.

3.2 Delay test of a Zn-Co battery

To evaluate the self-discharge behavior, a Zn-Co battery was tested in the voltage range of 1.4 to 1.9 V as reported [18]. After charging to 1.9 V at a low current density of 0.5 A g^{-1}, it was delayed for 10 h. As shown in Fig. 2a, the circuit-voltage dropped dramatically at first, then dropped steadily, and finally decreased to 1.7 V. Correspondingly, the discharge capacity decreased obviously from 220.4 to 158.6 mA h g^{-1} with a retention ratio of only 72%. It is worth noting that two voltage plateaus are displayed during the discharging process: a short one at ~1.7 V and a long one at ~1.6 V (Fig. S5), which may represent the valence state transformations from 4+ → 3+ and 3+ → 2+, respectively, well consistent with the CV results. Interestingly, the short one disappears after the delay, while the long one remains and almost overlaps with the pristine curve. Based on this phenomenon, it is first preliminarily speculated that the severe self-discharge behavior may be triggered by the oxygen evolution reaction (OER), which can occur upon charging when the voltage is higher than 1.65 V (vs. Zn) under the alkaline environment [9,49–51]. After charging, the negative electrode (i.e., Zn) may balance with O_2, leading to voltage attenuation. To validate this conjecture, the charge voltage was confined from 1.9 to 1.8, 1.7, and even 1.6 V. After the delay, the open-circuit voltage decreased to 1.68, 1.62, and 1.54 V, respectively, as shown in Fig. S5. Although the OER can hardly occur at 1.7 and 1.6 V, the corresponding voltage stability is still very poor (Fig. 2b). Further, more severe self-discharge behavior is found at a high current density of 10 A g^{-1} (Fig. S6). Hence, the poor capacity retention ability and the voltage decrease have no concern with the OER, which may be attributed to the poor valence retention capability.

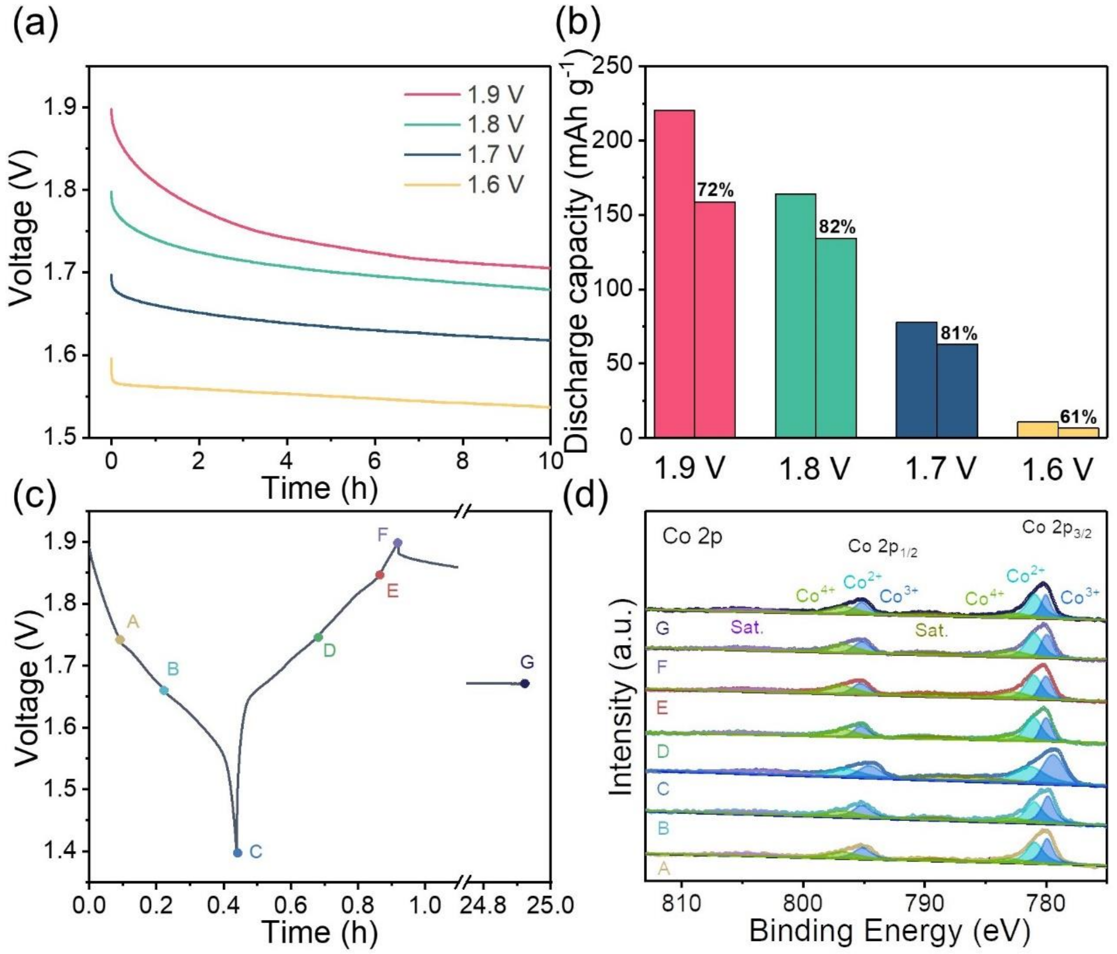

Fig. 2. (a) The voltage variation after charging to different voltages during the delay for 10 h and (b) the corresponding discharge capacities (left: pristine; right: after the delay). (c) Voltage-time curve and the selected points for test and (d) the corresponding Co 2p XPS spectra.

Based on the reaction mechanism of Co_3O_4, the valence state is proposed to vary from 2+ to 3+ and 4+ [23]. Fig. 2c shows the charge-discharge curves and the voltage variation during the delay for 24 h, and the endpoints of different voltage plateaus were selected to ex-situ investigate the valence state transformation. The XPS test is used to measure the valence state of the electrode surface. Although some other methods such as the inductively coupled plasma emission spectrometer (ICP) can be also used, the reaction with bulk during measurement will change the valence state, leading to inaccuracy. For other measurements like X-ray absorption near-edge spectroscopy (XANES) and electron paramagnetic resonance (EPR), they can measure the values accurately [26,52,53]. In this work, the valence state of cobalt oxide on the surface is vital to electrochemical performance. Although the XPS test can hardly give accurate values of the bulk material, it can well reflect the tendency of valence state variation near the electrode surface. More importantly, the operation of XPS is relatively easy. Hence, we chose XPS to test the surface state of the electrode material. For the Co_3O_4 grown on the Ni foam, the active material covers the nickel foam completely. During the charging and discharging processes, Ni foam can hardly contact the electrolyte. Hence, the Ni element is almost not involved in the spinel structure of Co_3O_4 and will not react during the charging/discharging process. In addition, Ni foam is a stable matrix and hardly reacts in alkaline electrolytes. Kong et al. reported that the CV curves of the Ni foam have almost no peak, indicating its negligible contribution to the overall performance [54]. As shown in Fig. S7, the XPS spectrum of the Co_3O_4 electrode gives the intensity of various elements. Obviously, the peak of the Co element is much stronger than the Ni element, and the Ni element may derive from the Ni foam substrate. Hence, the contribution of the Ni element to the charging/discharging reaction is ultralow. Fig. 2d shows the corresponding XPS spectra of Co 2p. Compared to Co^{2+} and Co^{3+}, Co^{4+} has a greater positive electrical charge and a lower density of electron cloud, therefore the binding energy of the electrons in the 2p orbital should also be larger [55,56]. Hence, Co^{2+} and Co^{3+} have relatively smaller binding energy than Co^{4+}. Based on the previous works, the peaks at 795.6 eV and 781.0 eV are attributable to Co^{2+}, the peaks at 794.9 eV and 779.7 eV are indexed to Co^{3+}, and the peaks at 796.4 eV and 781.5 eV correspond to Co^{4+} [57–59]. Table 1 summarizes the ratios of different valence states. As the discharge reaction progresses, the amount of Co^{2+} and Co^{3+} increases gradually, especially the Co^{2+}, while Co^{4+} decreases dramatically, and even disappears to the end, consistent with the CV results. When the electrode is charging from C to D, in contrast, Co^{4+} increases quickly to 28.26%, Co^{2+} and Co^{3+} decreases from 54.65% to 44.18% and 45.35% to 27.56%, respectively, demonstrating the fast oxidation of the active material. When charging from D to E, Co^{4+} continues to increase to 34.11%. While from E to F, Co^{4+} almost has no change, Co^{2+} decreases to 32.81% but Co^{3+} increases to 32.2%, further raising the average valence state. It is noting that a remarkable amount of Co^{2+} still exists even after charging to 1.9 V, which manifests that the full valence state transformation is hard to complete, leading to poor utilization, which may be restricted by the poor conductivity, low surface area, and the spinel structure [60]. After the delay for 24 h (G), Co^{4+} decreases dramatically from 34.99% to 28.80% but Co^{2+} and Co^{3+} increase, proving the instability of Co^{4+} under the delay state, which may be the key to the self-discharge behavior. Based on the experimental results, the self-discharge of the Co_3O_4 electrode involves the spontaneous transformation from a high to low valence state due to the instability of the high valence state [27]. In detail, it involves the reactions from CoO_2 to CoOOH and Co_3O_4. Hence, the oxidation state change in Co-ions during self-discharge is due to the spontaneous reduction of the high valence state (Co^{4+}). According to the fitting result of CV curves in Figs. 1d-f, the b-value is near 1.0 and the pseudocapacitive contribution ratio is up to 90%, demonstrating the pseudocapacitive contribution control in the redox reaction of the Zn-Co battery. This pseudocapacitance may be ascribed to the adsorption and desorption of some species on the electrode surface. Furthermore, since only two elements involve in the Co_3O_4 electrode, the charge compensating species to the oxidation state change in Co-ions during self-discharge may be the oxygen-based species. For instance, from the reaction mechanism, OH^- is correlated and may be absorbed on the surface of Co-based materials. During charging, the Co-ion can combine with $OH^–$ to form $Co(OH)_4$. While during the delay, $OH^–$ may be detached from the surface, which decreases the oxidation state in Co-ions, and therefore leading to the self-discharge. For this reason, we speculated that $OH^–$ may be detached from the surface during self-discharge, resulting in the reduction of the high valence state in Co-ions.

To understand the mechanism of self-discharge deeply, the reaction rate (k) under the delay conditions was investigated. The variation of the voltage with time during the self-discharge process can be obtained from the following differential equation [61]:

$$\frac{dV}{dt} + kV = 0 \tag{3}$$

Hence, k can be obtained according to the curve of voltage variation with time during self-discharge. According to the Tafel equation, the electron transfer rate, k can be also written as:

$$k = m \cdot \exp(\alpha FV / RT) \tag{4}$$

where m and α are constant, F is the Faraday constant (96485 C mol^{-1}), R is the gas constant (8.314 J K^{-1} mol^{-1}), and T is the temperature (K). As shown in Fig. S8, k can reach 8×10^{-5} 1/s at 1.9 V, while dramatically drops at first and gradually decreases to near 0, which indicates that the severe self-discharge at the beginning may be due to the diffusion of OH^{-}. According to the fitted result, m and α are calculated to be 5.24×10^{-23} 1/s and 0.57, respectively.

Table 1. Ratios of different components of the electrodes corresponding to Fig. 2d.

Electrodes	Co^{2+}	Co^{3+}	Co^{4+}	Valence state
A (Discharging to 1.75 V)	30.55%	41.78%	27.66%	2.97
B (Discharging to 1.65 V)	32.38%	42.62%	25.00%	2.93
C (Discharging to 1.40 V)	54.65%	45.35%	-	2.45
D (Charging to 1.75 V)	44.18%	27.56%	28.26%	2.84
E (Charging to 1.85 V)	35.63%	30.26%	34.11%	2.98
F (Charging to 1.90 V)	32.81%	32.20%	34.99%	3.02
G (After 24 h delay)	34.21%	36.99%	28.80%	2.95

3.3 Changing the charging protocol for a Zn-Co battery

In light of the above results, the increase of Co^{4+} on the present electrode is restricted through the galvanostatic charging from 1.4 to 1.9 V. To further improve the depth of valence state transformation, the potentiostatic charging to 1.9 V may be an efficient strategy. To this end, different time (i.e., 0.5, 1, 3, and 6 h) of potentiostatic charging was set after galvanostatic charging to 1.9 V at 0.5 A g^{-1}, and the self-discharge behaviors were tested. As illustrated in Fig. 3a, great improvement is achieved in the voltage attenuation during the delay, and the suppression effect gets more obvious with the time increasing from 0.5 to 3 h. More importantly, the discharge capacity increases distinctly after potentiostatic charging (Fig. 3b), which even reaches 290 mAh g^{-1} at 6 h owing to the further transformation that lifts the utilization, much higher than the previously reported one, such as Co_3O_4 nanosheet (162 mAh g^{-1}) and Co_3O_4 nanowire (174 mAh g^{-1}) (Table S1). Besides, the energy density increases from 367.7 to 491.6 Wh kg^{-1}, and the peak power density increases from 88.3 to 91.5 mW cm^{-2} (Fig. S9). Fig. 3c shows the XPS spectra comparison of the electrodes after potentiostatic charging for 6 h and normal galvanostatic charging. Obviously, the amount of Co^{4+} further increases from 34.99% to 37.69% after potentiostatic charging (Table 2). Further, the EIS results also show that both the ohmic and charge resistance decrease (Fig. S10), which may be ascribed to the increased high valence state [23,62]. At the voltage region of 1.4 to 1.8 V, the capacity increase and the suppression effect to the self-discharge were weak (Figs. S11 and S12). Additionally, the variations in the current density during the potentiostatic charging processes at 1.8 V (0.003 A g^{-1}) and 1.9 V (0.03 A g^{-1}) were also different (Fig. S13). The above phenomena demonstrate that the cobalt ion with a high valence can be further transformed under a higher voltage region through the potentiostatic charging. Hence, changing the charging protocol can effectively increase the valence state, which can also alleviate capacity decay after the delay. As shown in Fig. 3d, the capacity retention ratio after delay for 10 h increases from 72% to 84%, 87%, 90%, and 90% as the potentiostatic time increases from 0 to 0.5, 1, 3, and 6 h. Noted that this value is calculated based on the potentiostatic charging and after delay. Actually, the capacity after delay can be even higher than the pristine one after galvanostatic charging from 1.4 to 1.9 V. Interestingly, the shape of discharge curves also changed (Fig. 3b). Since the valence state transformation during discharging involves Co^{4+} to Co^{3+} and Co^{3+} to Co^{2+}, the discharge process displays two voltage plateaus [23]. With an increase of the potentiostatic charging time, the amount of Co^{4+} increases. Therefore, the high voltage plateau extends and the discharge curves become more flat, leading to the shape changes. With the potentiostatic time increases, the high voltage plateau rises obviously and becomes longer, indicating the lift in the high valence state. Even after delay, the high voltage plateau can still remain, which is elevated dramatically up to 1.75 V, enough to drive the high valence state transformation and thus can retain more capacity. When the potentiostatic time reaches 3 h, the capacity retention ratio remains at ~90%, which demonstrates that the time is relevant to the remaining voltage. It is noted that after further increasing the potentiostatic charging time from 3 to 6 h, the voltage variation during the delay did not change and almost overlapped. Hence, the remaining voltage will not further increase when the potentiostatic charging time increases. Since the remaining voltage is the driving force for the discharge process, the capacity retention ratio will also not change when further increasing the potentiostatic charging time after 3 h. From the overall consideration, the great effect of this new charging protocol on suppressing self-discharge and lifting capacity can be attributed to the following reasons: Ⅰ) the high valence state can only transform thoroughly when charging under a high voltage region; Ⅱ) the potentiostatic charging process ensures the sufficient valence state transformation, thus increasing the amount of high valence state dramatically; Ⅲ) the high voltage plateau will become longer as an increase in the high valence state; Ⅳ) the remaining voltage after the delay will improve up to 1.75 V since more high valence state can reserve, and the high voltage could drive the utilization of species thoroughly. For the conventional charging protocol (i.e., galvanostatic charging), however, it is hard to obtain the sufficient high valence state due to the limiting conversion ability. Therefore, the high discharge voltage plateau corresponding to Co^{4+} to Co^{3+} is restricted, leading to the poor utilization of the active material and low discharge voltage plateau. After the delay, the voltage decreases rapidly, which can not afford the high valence state transformation, causing poor capacity retention. Noted that this strategy is different from the electrochemical activation using the CV method conducted in the fixed potential range, which is mainly benefited from the optimal reaction interface between the electrolyte and the electrode while not involving the valance state variation [63]. Although this charging protocol has been reported for some supercapacitors, the optimization mechanism is not the same [64]. For the supercapacitors, a further potentiostatic charging can alleviate the charge redistribution due to the inequality during charging and make the charged ions distributed uniformly, restricting the self-discharge. Hence, this work proposes a novel strategy to improve the performance of the Zn-Co battery and restrict its self-discharge based on a new mechanism, which may pave a road for the development of Zn batteries. However, too long time is also a barrier for practical operation. To further investigate the effect of time, the cycle behaviors after potentiostatic charging for 3 and 6 h were tested. As shown in Fig. 3e-f, severe attenuation of capacity occurs after potentiostatic charging for 6 h, while the battery can operate well for 3 h. The SEM images of the Co_3O_4 electrode after potentiostatic charging for 6 h are shown in Fig. S14. The microstructure of the nanowire has collapsed and broken, which may be due to the over-charge and aggregation of oxygen/hydrogen bubbles. Therefore, the specific surface area decreased and the pore structure collapsed, leading to the poor utilization of active material and insufficient contact between the electrolyte. On the other hand, although the high conversion depth of Co^{4+} can be achieved after long-time potentiostatic charging, it can not be recovered completely under the conventional charging protocol since Co^{4+} is unstable. For this reason, the battery after a longer potentiostatic charging time shows poor stability. Thereafter, selecting the reasonable time for potentiostatic charging is of vital importance.

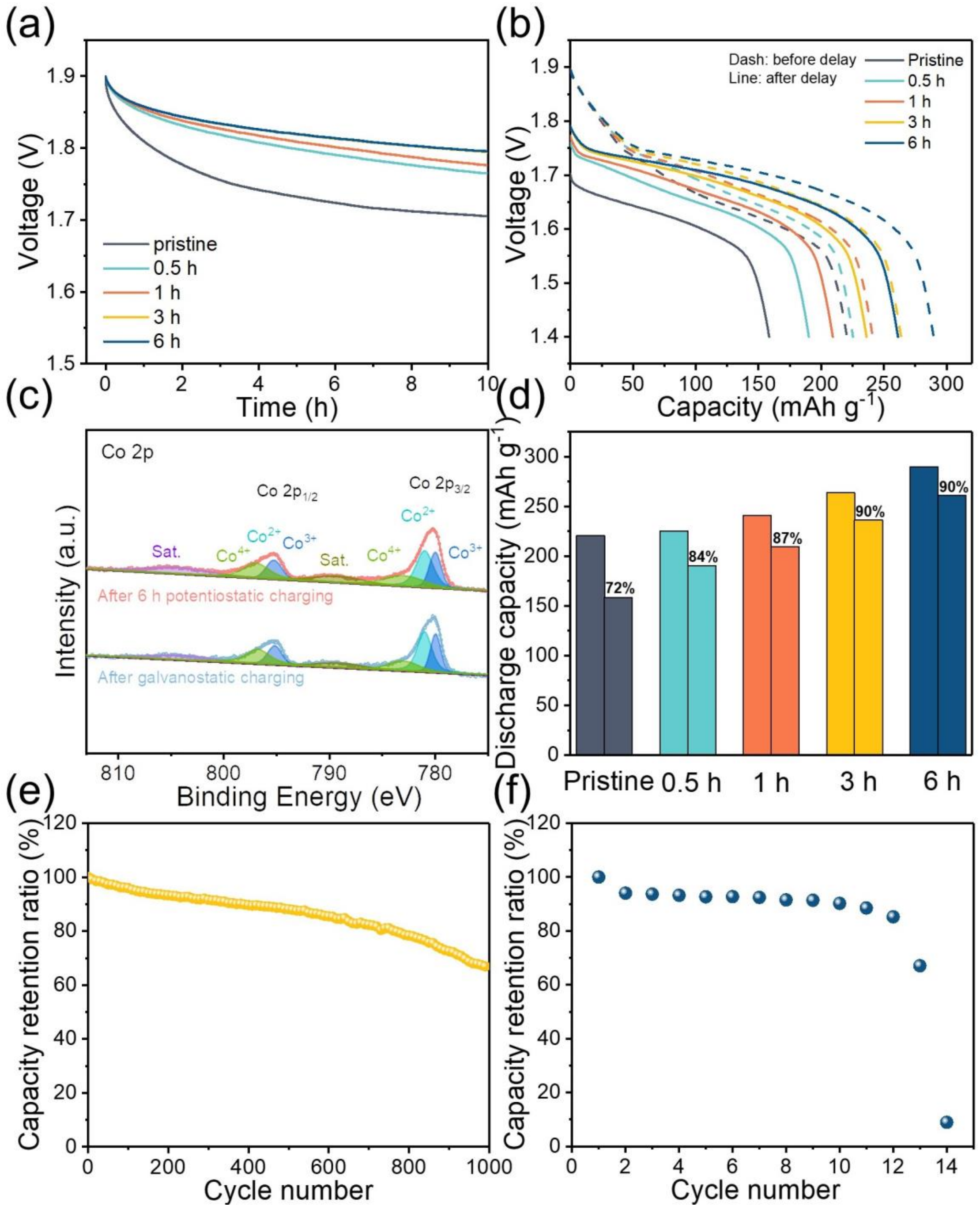

Fig. 3. The battery performance under the potentiostatic charging protocol: (a) The voltage variations using different potentiostatic charging time during 10 h delay. (b) the discharge curves before and after potentiostatic charging. (c) the Co 2p XPS spectra after 6 h potentiostatic charging and after charging. (d) the corresponding discharge capacities (left: pristine; right: after delay). The capacity retention ratios

during cycles after potentiostatic charging for (e) 3 h and (f) 6 h.

Table 2. Ratios of different components of the electrodes corresponding to Fig. 3c.

Electrode	Co^{2+}	Co^{3+}	Co^{4+}	Valence state
After 6 h potentiostatic charging	30.85%	31.46%	37.69%	3.07
After galvanostatic charging	32.81%	32.20%	34.99%	3.02

3.4 Selecting the optimal charge-discharge voltage region

From the XPS results, the cobalt ions in different voltage regions exhibit distinctive valence transformation ability. Thereafter, it is vital to select a reasonable charge-discharge voltage region. Considering the poor cycle stability under the low voltage region in which the corresponding valence state transformation is unstable, the optimal cycling operation region is still selected from 1.4 to 1.9 V (Fig. S15). Since the oxidation from Co^{2+} to Co^{3+} and Co^{3+} to Co^{4+} occur at ~1.7 V and ~1.85 V, respectively, the choice of cut-off charging voltage is related to the conversion level of the valence state. Therefore, the high valence state can transform effectively when charging to a high voltage (e.g., 1.9 V), while the transformation is not sufficient when the cut-off charging voltage decreases, leading to the capacity retention ratio decreases from 76% to 44% when the cut-off voltage decreases from 1.9 to 1.8 V. Although further increasing the charging cut-off voltage may develop the stability, severe hydrogen evolution reaction (HER) and OER will also occur. For a Zn-Co battery with a closed system, the OER will lift the air pressure in the electrolyte, leading to leakage and damage of the electrode [65–67]. Hence, in this work, the cut-off voltage was set at 1.9 V to suppress the OER [13]. Additionally, the voltage decreases rapidly below 1.5 V because the insufficient ion transport, therefore the deep discharge may damage the reaction interfaces. Hence, the cycle including the potentiostatic charging under a reasonable voltage region may be an effective strategy to utilize the valence state transformation. To investigate the performance of this new cycle mode, 10 min potentiostatic charging was selected since too long potentiostatic charging time is a waste of electric energy and time and the current density becomes stable within 10 min (Fig. S16). Besides, the galvanostatic charging and discharging were set at 2 A g^{-1}. As shown in Fig. S17, including 10 min potentiostatic charging, the initial capacity is 212 mA h g^{-1}, while it changes to 255, 251, 226, and 208 mA h g^{-1} at the 500th, 1000th, 2000th, 2500th cycle, respectively. Significantly, the coulombic efficiency is only 90.2% initially, and increases to ~97% after the 250th cycle and remains stable, manifesting the decent energy conversion efficiency during the subsequent cycles. From Fig. 4, the capacity retention ratio increases gradually at first, then reaches the max value of 121% (257 mA h g^{-1}) at the 600th cycle and remains well until the 1000th cycle. It is noted that the high valance state of Co can be further lifted after the potentiostatic charging, therefore the utilization of active material can be gradually activated with the cycle, which leads to the dramatic capacity increase during the first 600 cycles. Subsequently, the value decreases slowly and can still reach 100% before the 2500th cycle (over 1000 h), much better than the previously reported one (Table S1), which indicates that the stability did not sacrifice after using this charging protocol. Although the redox pair of Co^{3+}/Co^{4+} is unstable as mentioned in previous literature [25–27], the sufficient conversion towards Co^{4+} during the charging process can offset the degradation of Co^{4+}, which leads to the maintenance of cycling stability. After that, however, the value drops rapidly after the 2500th cycle (Fig. S18) attributed to the severe Zn electrode issues (Fig. S19) because of the too-long operation time (over 1200 h), which may be further optimized by replacing the Zn plate without changing other condition. In comparison, for the battery without potentiostatic charging, the capacity retention ratio decreases gradually and finally reaches only 73% at the 2500th cycle (only 500 h) [18]. Furthermore, the poor cycle behavior for the voltage region of 1.4 to 1.8 V also validates the insufficient valence transformation under a low voltage region (Fig. S20).

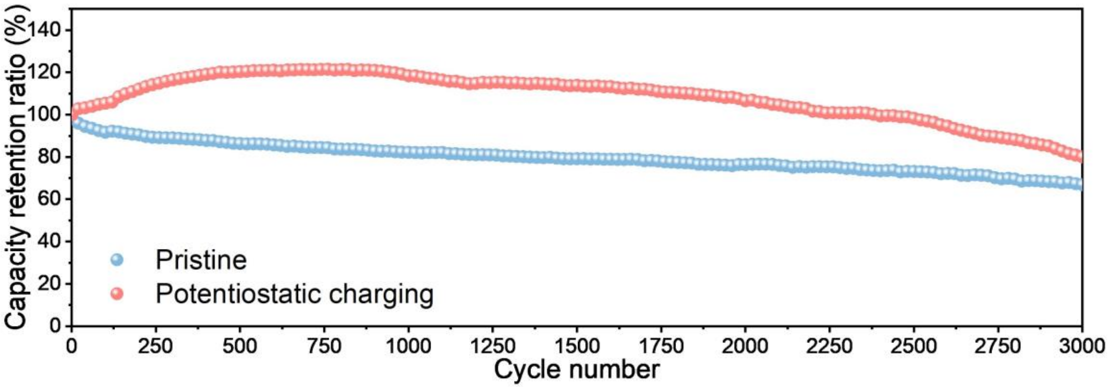

Fig. 4. The capacity retention ratios during 2500 cycles for the Zn-Co battery with 10 min potentiostatic charging and pristine one.

4. Conclusions

In summary, the self-discharge behavior of a Zn-Co battery was investigated systematically. Under the typical charging mode, the high state valence (Co^{4+}) is difficult to convert thoroughly, leading to the short high-voltage plateau. During the delay process, the unstable high valence state leads to the fast decrease of the voltage, causing severe capacity attenuation. After potentiostatic charging, the amount of high valence state increases dramatically, and the discharge capacity even lifts to 290 mAh g^{-1}. Moreover, the remaining voltage increases effectively after delay, and the high voltage region can reserve well, effectively improving the capacity retention ratio from 72% to 90%. As for the cycling stability, an optimal charge-discharge voltage region from 1.4 to 1.9 V was selected. Through including the 10 min potentiostatic charging, the capacity retention ratio can increase gradually to 121% until the 600th cycle, and the battery can operate well for 2500 cycles (over 1000 h) with almost no decay. Thus, through the potentiostatic charging, the amount of the high valence state increases dramatically, leading to the high voltage region reservation, and therefore effectively alleviating the self-discharge. This strategy is also convenient and does not require modification of the internal structure of the battery. Thus, this work provides a simple and effective method that can alleviate self-discharge to a large extent, shedding light on the development of Zn-Co batteries. In future research, the strategies started from the material level and the operating management level are needed to realize high-performance batteries.

CRediT authorship contribution statement

Wenxu Shang: Conceptualization, Investigation, Methodology, Writing - original draft. **Wentao Yu:** Investigation, Methodology. **Xu Xiao:** Investigation. **Yanyi Ma:** Investigation. **Ziqi Chen:** Investigation. **Meng Ni:** Writing - review & editing, Supervision, Funding acquisition. **Peng Tan:** Conceptualization, Formal analysis, Writing - review & editing, Supervision, Project administration, Funding acquisition.

Declaration of Competing Interest

A Chinese Patent related to this work has been filed.

Acknowledgements

P. Tan thanks the funding support from Anhui Provincial Natural Science Foundation (2008085ME155), USTC Research Funds of the Double First-Class Initiative (YD2090002006), Joint Laboratory for USTC and Yanchang Petroleum (ES2090130110), Chinese Academy of Sciences (CAS) Program (KJ2090130001), and USTC Tang Scholar (KY2090000065). M. Ni thanks the funding support (Project Number: PolyU 152214/17E and PolyU 152064/18E) from Research Grant Council, University Grants Committee, Hong Kong SAR.

References

[1] Yoshino A. The birth of the lithium-ion battery. Angew Chemie, Int Ed 2012;51:5798–800.

[2] Shin J, Choi JW. Opportunities and Reality of Aqueous Rechargeable Batteries. Adv Energy Mater 2020;10:2001386.

[3] Wang Q, Yang H, Meng T, Yang J, Huang B, Gu FL, et al. Boosting Electron Transfer with Heterointerface Effect for High-Performance Lithium-Ion Storage. Energy Storage Mater 2021;36:365–75.

[4] Han X, Lu L, Zheng Y, Feng X, Li Z, Li J, et al. A review on the key issues of the lithium ion battery degradation among the whole life cycle. ETransportation 2019;1:100005.

[5] Wang Q, Jiang L, Yu Y, Sun J. Progress of enhancing the safety of lithium ion

battery from the electrolyte aspect. Nano Energy 2019;55:93–114.

[6] Ouyang D, Chen M, Huang Q, Weng J, Wang Z, Wang J. A Review on the thermal hazards of the lithium-ion battery and the corresponding countermeasures. Appl Sci 2019;9:2483.

[7] Yi J, Liang P, Liu X, Wu K, Liu Y, Wang Y, et al. Challenges, mitigation strategies and perspectives in development of zinc-electrode materials and fabrication for rechargeable zinc-air batteries. Energy Environ Sci 2018;11:3075–95.

[8] Li H, Ma L, Han C, Wang Z, Liu Z, Tang Z, et al. Advanced rechargeable zinc-based batteries: Recent progress and future perspectives. Nano Energy 2019;62:550–87.

[9] Tan P, Chen B, Xu H, Zhang H, Cai W, Ni M, et al. Flexible Zn- and Li-air batteries: Recent advances, challenges, and future perspectives. Energy Environ Sci 2017;10:2056–80.

[10] Shang W, Yu W, Tan P, Chen B, Xu H, Ni M. A high-performance Zn battery based on self-assembled nanostructured $NiCo_2O_4$ electrode. J Power Sources 2019;421:6–13.

[11] Shang W, Yu W, Liu Y, Li R, Dai Y, Cheng C, et al. Rechargeable alkaline zinc batteries: Progress and challenges. Energy Storage Mater 2020;31:44–57.

[12] Liu Z, Luo X, Qin L, Fang G, Liang S. Progress and prospect of low-temperature zinc metal batteries. Adv Powder Mater 2020. Doi:10.1016/j.apmate.2021.10.002

[13] Wang X, Wang F, Wang L, Li M, Wang Y, Chen B, et al. An Aqueous Rechargeable Zn//Co_3O_4 Battery with High Energy Density and Good Cycling Behavior. Adv Mater 2016;28:4904–11.

[14] Jiang HR, Wu MC, Ren YX, Shyy W, Zhao TS. Towards a uniform distribution of zinc in the negative electrode for zinc bromine flow batteries. Appl Energy 2018;213:366–74.

[15] Xu N, Zhang Y, Wang Y, Wang M, Su T, Coco CA, et al. Hierarchical bifunctional catalysts with tailored catalytic activity for high-energy rechargeable Zn-air batteries. Appl Energy 2020;279:115876.

[16] Pan L, Chen D, Pei P, Huang S, Ren P, Song X. A novel structural design of air cathodes expanding three-phase reaction interfaces for zinc-air batteries. Appl Energy 2021;290:116777.

[17] Tan P, Chen B, Xu H, Cai W, He W, Ni M. In-situ growth of Co_3O_4 nanowire-assembled clusters on nickel foam for aqueous rechargeable Zn-Co_3O_4 and Zn-air batteries. Appl Catal B Environ 2019;241:104–12.

[18] Shang W, Yu W, Xiao X, Ma Y, Cheng C, Dai Y, et al. Microstructure-tuned cobalt oxide electrodes for high-performance Zn-Co batteries. Electrochim Acta 2020;353:136535.

[19] Wang H, Zhou Y, Zhang S, Deng C. Engineering the defects of Co_3O_{4-x} bubbles in lotus root-like multichannel nanofibers to realize superior performance and high durability for fiber-shaped hybrid Zn battery. Chem Eng J 2020;407:127043.

[20] Shang W, Yu W, Xiao X, Ma Y, Tan P, Ni M. Unravel the influences of Ni substitution on Co-based electrodes for rechargeable alkaline Zn-Co batteries. J Power Sources 2021;483:229192.

[21] Li Q, Zhang Q, Zhou Z, Gong W, Liu C, Feng Y, et al. Boosting Zn-ion storage capability of self-standing Zn-doped Co_3O_4 nanowire array as advanced cathodes for high-performance wearable aqueous rechargeable Co//Zn batteries. Nano Res 2021;14:91–9.

[22] Xie Y, Fei B, Cai D, Chen Q, Cui Z, Wang Q, et al. Multicomponent hierarchical $NiCo_2O_4@CoMoO_4@Co_3O_4$ arrayed structures for high areal energy density aqueous NiCo//Zn batteries. Energy Storage Mater 2020;31:27–35.

[23] Tan P, Chen B, Xu H, Cai W, He W, Liu M, et al. Co_3O_4 Nanosheets as Active Material for Hybrid Zn Batteries. Small 2018;14:1800225.

[24] Tan P, Chen B, Xu H, Cai W, He W, Ni M. Investigation on the electrode design of hybrid Zn-Co_3O_4/air batteries for performance improvements. Electrochim Acta 2018;283:1028–36.

[25] Huang M, Li M, Niu C, Li Q, Mai L. Recent Advances in Rational Electrode Designs for High-Performance Alkaline Rechargeable Batteries. Adv Funct Mater 2019;29:1807847.

[26] Zeng Y, Lai Z, Han Y, Zhang H, Xie S, Lu X. Oxygen-Vacancy and Surface Modulation of Ultrathin Nickel Cobaltite Nanosheets as a High-Energy Cathode for Advanced Zn-Ion Batteries. Adv Mater 2018;30:1–8.

[27] Tang Y, Li X, Lv H, Xie D, Wang W, Zhi C, et al. Stabilized Co^{3+}/Co^{4+} Redox Pair in In Situ Produced $CoSe_{2-x}$-Derived Cobalt Oxides for Alkaline Zn Batteries with 10 000-Cycle Lifespan and 1.9-V Voltage Plateau. Adv Energy Mater 2020;10:2000892.

[28] Ricketts BW, Ton-That C. Self-discharge of carbon-based supercapacitors with organic electrolytes. J Power Sources 2000;89:64–9.

[29] Wang H, Zhou Q, Yao B, Ma H, Zhang M, Li C, et al. Suppressing the Self-Discharge of Supercapacitors by Modifying Separators with an Ionic Polyelectrolyte. Adv Mater Interfaces 2018;5:1–7.

[30] Wang Q, Zhang Y, Jiang H, Li X, Cheng Y, Meng C. Designed mesoporous hollow sphere architecture metal (Mn, Co, Ni) silicate: A potential electrode material for flexible all solid-state asymmetric supercapacitor. Chem Eng J 2019;362:818–29.

[31] Yang X-G, Liaw BY. Self-Discharge and Charge Retention in AB_2-Based Nickel Metal Hydride Batteries. J Electrochem Soc 2004;151:A137–43.

[32] Choi SH, Kim J, Yoon YS. Self-discharge analysis of $LiCoO_2$ for lithium batteries. J Power Sources 2004;138:283–7.

[33] Xia M, Nie J, Zhang Z, Lu X, Wang ZL. Suppressing self-discharge of supercapacitors via electrorheological effect of liquid crystals. Nano Energy 2018;47:43–50.

[34] Peng H, Xiao L, Sun K, Ma G, Wei G, Lei Z. Preparation of a cheap and environmentally friendly separator by coaxial electrospinning toward

suppressing self-discharge of supercapacitors. J Power Sources 2019;435:226800.

[35] Chen L, Bai H, Huang Z, Li L. Mechanism investigation and suppression of self-discharge in active electrolyte enhanced supercapacitors. Energy Environ Sci 2014;7:1750–9.

[36] Di Blasi A, Busaccaa C, Di Blasia O, Briguglio N, Squadrito G, Antonuccia V. Synthesis of flexible electrodes based on electrospun carbon nanofibers with Mn3O4nanoparticles for vanadium redox flow battery application. Appl Energy 2017;190:165–71.

[37] Pei P, Wang K, Ma Z. Technologies for extending zinc–air battery's cycle life: A review. Appl Energy 2014;128:315–24.

[38] Liao X, Sun P, Xu M, Xing L, Liao Y, Zhang L, et al. Application of tris(trimethylsilyl)borate to suppress self-discharge of layered nickel cobalt manganese oxide for high energy battery. Appl Energy 2016;175:505–11.

[39] Bardé F, Palacín MR, Beaudoin B, Christian PA, Tarascon JM. Cationic substitution in γ-type nickel (oxi)hydroxides as a means to prevent self-discharge in Ni/Zn primary batteries. J Power Sources 2006;160:733–43.

[40] Arcos-Vargas Á, Canca D, Núñez F. Impact of battery technological progress on electricity arbitrage: An application to the Iberian market. Appl Energy 2020;260:114273.

[41] Xiong R, Li L, Li Z, Yu Q, Mu H. An electrochemical model based degradation state identification method of Lithium-ion battery for all-climate

electric vehicles application. Appl Energy 2018;219:264–75.

[42] Jaguemont J, Boulon L, Dubé Y. A comprehensive review of lithium-ion batteries used in hybrid and electric vehicles at cold temperatures. Appl Energy 2016;164:99–114.

[43] Zhang H, Song X, Xia T, Yuan M, Fan Z, Shibasaki R, et al. Battery electric vehicles in Japan: Human mobile behavior based adoption potential analysis and policy target response. Appl Energy 2018;220:527–35.

[44] Andreas HA. Self-Discharge in Electrochemical Capacitors: A Perspective Article. J Electrochem Soc 2015;162:A5047–53.

[45] Kim SH, Miesse CM, Lee HB, Chang IW, Hwang YS, Jang JH, et al. Ultra compact direct hydrogen fuel cell prototype using a metal hydride hydrogen storage tank for a mobile phone. Appl Energy 2014;134:382–91.

[46] Mao Y, Xie J, Liu H, Hu W. Hierarchical Core-shell Ag@Ni$(OH)_2$@PPy Nanowire Electrode for Ultrahigh Energy Density Asymmetric Supercapacitor. Chem Eng J 2020;405:126984.

[47] Nkeng P, Poillerat G, Koenig JF, Chartier P, Lefez B, Lopitaux J, et al. Characterization of Spinel- Type Cobalt and Nickel Oxide Thin Films by X- Ray Near Grazing Diffraction, Transmission and Reflectance Spectroscopies, and Cyclic Voltammetry. J Electrochem Soc 1995;142:1777–83.

[48] Casella IG, Gatta M. Study of the electrochemical deposition and properties of cobalt oxide species in citrate alkaline solutions. J Electroanal Chem

2002;534:31–8.

[49] Fu J, Liang R, Liu G, Yu A, Bai Z, Yang L, et al. Recent Progress in Electrically Rechargeable Zinc–Air Batteries. Adv Mater 2018;29:1805230.

[50] Fu J, Cano ZP, Park MG, Yu A, Fowler M, Chen Z. Electrically Rechargeable Zinc–Air Batteries: Progress, Challenges, and Perspectives. Adv Mater 2017;29:1604685.

[51] Shang W, Yu W, Tan P, Chen B, Wu Z, Xu H, et al. Achieving high energy density and efficiency through integration: Progress in hybrid zinc batteries. J Mater Chem A 2019;7:15564–74.

[52] An L, Huang B, Zhang Y, Wang R, Zhang N, Dai T, et al. Interfacial Defect Engineering for Improved Portable Zinc–Air Batteries with a Broad Working Temperature. Angew Chemie - Int Ed 2019;58:9459–63.

[53] Li MS, Lin ZY, Chen QW. Metal-organic frameworks derived Ag-$CoSO_4$ nanohybrids as efficient electrocatalyst for oxygen evolution reaction. Chinese J Chem Phys 2019;32:731–8.

[54] Kong D, Luo J, Wang Y, Ren W, Yu T, Luo Y, et al. Three-dimensional Co_3O_4@MnO_2 hierarchical nanoneedle arrays: Morphology control and electrochemical energy storage. Adv Funct Mater 2014;24:3815–26.

[55] Lu Y, Chen L, Lu C, Ni Y, Xu Z. Effects of oxygen defects on structure and properties of $Sm_{0.5}Sr_{0.5}CoO_{3-\delta}$ annealed in different atmospheres. J Rare Earths 2013;31:1183–90.

[56] Xiong F, Zhou D, Xie Z, Chen Y. A study of the Ce^{3+}/Ce^{4+} redox couple in

sulfamic acid for redox battery application. Appl Energy 2012;99:291–6.

[57] Zhang R, Lu Y, Wei L, Fang Z, Lu C, Ni Y, et al. Synthesis and conductivity properties of $Gd_{0.8}Ca_{0.2}BaCo_2O_{5+\delta}$ double perovskite by sol–gel combustion. J Mater Sci Mater Electron 2015;26:9941–8.

[58] Lu Y, Sun L, Wei L, Zhang R, Lu C, Ni Y, et al. Influence of annealing atmosphere on the electrical and spectral properties of $Gd_{0.8}Ca_{0.2}BaCo_2O_{5+\delta}$ ceramic. J Mater Sci 2017;52:3794–805.

[59] Dupin J., Gonbeau D, Benqlilou-Moudden H, Vinatier P, Levasseur A. XPS analysis of new lithium cobalt oxide thin-films before and after lithium deintercalation. Thin Solid Films 2001;384:23–32.

[60] Ji D, Fan L, Tao L, Sun Y, Li M, Yang G, et al. Kirkendall Effect for Engineering Oxygen Vacancy of Hollow Co_3O_4 Nanoparticles toward High-Performance Portable Zinc-air Batteries. Angew Chemie Int Ed 2019;58:13840–4.

[61] Tevi T, Takshi A. Modeling and simulation study of the self-discharge in supercapacitors in presence of a blocking layer. J Power Sources 2015;273:857–62.

[62] He D, Song X, Li W, Tang C, Liu J, Ke Z, et al. Active electron density modulation of Co_3O_4 based catalysts endows highly oxygen evolution capability. Angew Chemie, Int Ed 2020;59:2–9.

[63] Davis MA, Andreas HA. Identification and isolation of carbon oxidation and charge redistribution as self-discharge mechanisms in reduced graphene oxide

electrochemical capacitor electrodes. Carbon N Y 2018;139:299–308.

[64] Haque M, Li Q, Smith AD, Kuzmenko V, Rudquist P, Lundgren P, et al. Self-discharge and leakage current mitigation of neutral aqueous-based supercapacitor by means of liquid crystal additive. J Power Sources 2020;453:227897.

[65] Aremu EO, Ryu K-S. Performance and degradation behavior of carbonyl Fe – MoS_2 composite as anode material in Fe-air batteries. Electrochim Acta 2019;313:468–77.

[66] Wang Z, Huang J, Guo Z, Dong X, Liu Y, Wang Y, et al. A Metal-Organic Framework Host for Highly Reversible Dendrite-free Zinc Metal Anodes. Joule 2019;3:1289–300.

[67] Zhang YQ, Tao HB, Chen Z, Li M, Sun YF, Hua B, et al. In situ grown cobalt phosphide (CoP) on perovskite nanofibers as an optimized trifunctional electrocatalyst for Zn-Air batteries and overall water splitting. J Mater Chem A 2019;7:26607–17.